Zuse Institute Berlin

Takustr. 7
14195 Berlin
Germany

J. TITSCHACK, D. BAUM, K. MATSUYAMA, K. BOOS,
C. FÄRBER, W.-A. KAHL, K. EHRIG, D. MEINEL,
C. SORIANO, S.R. STOCK

Ambient occlusion - a powerful algorithm to segment shell and skeletal intrapores in computed tomography data

The manuscript will appear in a slightly modified version in Computers & Geosciences.

Zuse Institute Berlin
Takustr. 7
14195 Berlin
Germany

Telephone: +49 30-84185-0
Telefax: +49 30-84185-125

E-mail: bibliothek@zib.de
URL: http://www.zib.de

ZIB-Report (Print) ISSN 1438-0064
ZIB-Report (Internet) ISSN 2192-7782

Ambient occlusion – a powerful algorithm to segment shell and skeletal intrapores in computed tomography data

Titschack, J.[1,2], Baum, D.[3], Matsuyama, K.[2], Boos, K.[1], Färber, C.[2], Kahl, W.-A.[4], Ehrig, K.[5], Meinel, D.[5], Soriano, C.[6], Stock, S.R.[7]

[1] MARUM – Center of Marine Environmental Sciences, University of Bremen, Leobener Straße 8, 28359 Bremen, Germany

[2] SaM – Senckenberg am Meer, Abteilung Meeresforschung, Südstrand 40, 26382 Wilhelmshaven, Germany

[3] ZIB – Zuse Institute Berlin, Takustraße 7, 14195 Berlin-Dahlem, Germany

[4] Department of Geosciences, University of Bremen, Klagenfurter Straße 2-4, 28359 Bremen, Germany

[5] BAM - Bundesanstalt für Materialforschung und -prüfung, Devision 8.5, Unter den Eichen 87, 12205 Berlin, Germany

[6] Advanced Photon Source, Argonne National Laboratory, 9700 South Cass Avenue, Argonne, IL 60439, USA

[7] Feinberg School of Medicine, Northwestern University, Abbott Hall Suite 810, 710 N Lake Shore Drive, Chicago IL 60611, USA

Corresponding author: Jürgen Titschack
jtitschack@marum.de
phone +49 (0)421 218 65623
fax +49 (0)421 218 9865623

Abstract

During the last decades, X-ray (micro-)computed tomography has gained increasing attention for the description of porous skeletal and shell structures of various organism groups. However, their quantitative analysis is often hampered by the difficulty to discriminate cavities and pores within the object from the surrounding region.

Herein, we test the ambient occlusion (AO) algorithm and newly implemented optimisations for the segmentation of cavities (implemented in the software Amira). The segmentation

accuracy is evaluated as a function of (i) changes in the ray length input variable, and (ii) the usage of AO (scalar) field and other AO-derived (scalar) fields. The results clearly indicate that the AO field itself outperforms all other AO-derived fields in terms of segmentation accuracy and robustness against variations in the ray length input variable. The newly implemented optimisations improved the AO field-based segmentation only slightly, while the segmentations based on the AO-derived fields improved considerably.

Additionally, we evaluated the potential of the AO field and AO-derived fields for the separation and classification of cavities as well as skeletal structures by comparing them with commonly used distance-map-based segmentations. For this, we tested the zooid separation within a bryozoan colony, the stereom classification of an ophiuroid tooth, the separation of bioerosion traces within a marble block and the calice (central cavity)-pore separation within a dendrophyllid coral. The obtained results clearly indicate that the ideal input field depends on the three-dimensional morphology of the object of interest. The segmentations based on the AO-derived fields often provided cavity separations and skeleton classifications that were superior to or impossible to obtain with commonly used distance-map-based segmentations. The combined usage of various AO-derived fields by supervised or unsupervised segmentation algorithms might provide a promising target for future research to further improve the results for this kind of high-end data segmentation and classification. Furthermore, the application of the developed segmentation algorithm is not restricted to X-ray (micro-)computed tomographic data but may potentially be useful for the segmentation of 3D volume data from other sources.

Keywords: computed tomography, micro-computed tomography, pore/cavity segmentation, ambient occlusion segmentation, pore/cavity/skeletal classification and separation

1. Introduction

X-ray computed tomography (CT) analyses have become a common tool in geo-biological research with various kinds of application (e.g., Cnudde *et al.*, 2006; Mees *et al.*, 2003; Stock, 2008a, b) including the visualisation and characterisation of cavities (pores) in solid media (e.g., Knackstedt *et al.*, 2008; Long *et al.*, 2009; Taina *et al.*, 2008). Thereby, three-dimensional (3D) high-resolution CT data provide non-destructive insights into the microstructure of organisms and exhibit the potential to elucidate the 3D distribution of different microstructures, especially of cavity (pore) systems (e.g., Morales Pinzón *et al.*, 2014; Sentoku *et al.*, 2015). For some of these analyses, the discrimination of the cavities from an object-surrounding space, both

commonly consisting of the same material, is crucial and difficult to obtain due to an irregular sample surface and a variable cavity opening at the object's surface – a problem that is not restricted to 3D CT data, but that occurs also in 3D volume datasets of other origin (e.g, Fredrich, 1999; Eicken *et al.*, 2000). Consequently, a specific and reproducible criterion for their discrimination should be used.

This study explores the ambient occlusion (AO) algorithm, which was recently introduced as segmentation tool by Baum and Titschack (2016) for the segmentation of cavities in natural materials. Presently, we (i) introduce and evaluate further improvements of the AO algorithm; (ii) test the accuracy of the cavity segmentation based on the AO (scalar) field and AO-derived (scalar) fields, i.e. the *AO average distance* field and the *AO eigenvalue* fields, and its dependency on variable ray length input parameters; and (iii) explore the potential of different AO-derived fields for the separation and classification of complex 3D cavities and skeletal structures. To gain a detailed insight into the first two aspects, we selected a bryozoan specimen that exhibits a high variability in the cavity-opening and surface morphology. For the third aspect, we selected four samples with highly different pore/skeletal structures: (i) the zooidal cavities of the bryozoan *Cellaria bafouri*; (ii) the tooth stereom of the ophiuroid *Amphiura filiformis*; (iii) sponge bioerosion traces (*Entobia* ispp.) within a marble block; and (iv) the calice (central corallite cavity) and pore network within the theca of the deep-water coral *Dendrophyllia* sp.

2. Ambient occlusion

The concept of AO was introduced by Zhukov *et al.* (1998; they referred to it as 'obscurence') to simulate indirect diffuse illumination for the visualisation of 3D scenes (see also Dachsbacher *et al.*, 2007 who referred to it as 'antiradiance'). The concept inverts the principle of light-exposure of a point in space to its obscurence by its close environment which was defined "*as the ratio of rays emanating from a point on the surface that are able to escape the scene*" by Loos and Sloan (2010; p. 2). The principle is used to calculate soft shadowing in 3D scenes and animation movies (e.g., Landis, 2002; Zhukov *et al.*, 1998) and to improve the rendering of isosurfaces and volumetric models (e.g., Borland, 2011; Penner and Mitchell, 2008; Tarini *et al.*, 2006). Correa and Kwan-Liu (2009) used the concept as classification algorithm for volumetric objects to enhance volume rendering by encoding the average contribution of the surrounding neighbourhood to the visibility of every voxel in a volume. In contrast to these authors, Baum and Titschack (2016) used the concept of AO to separate the empty space inside an object from the empty space surrounding the object – a typical problem

within 3D volume data of porous objects. For this, the object itself needs to be segmented. The resulting binary scalar field separates foreground (object) and background. The AO algorithm emits a predefined number of rays with a predefined length from every background voxel (cavity and surrounding space) of the produced binary field isotropically in all directions and counts the relative number of rays that touch or penetrate the foreground (Fig. 1). The obtained values are written into the new *AO field* at the position of the voxel from which the rays were emitted. The AO algorithm also computes the intersection points of the emitted rays with the foreground. From this information, several other AO-derived fields are computed. First, the average distance of each voxel to its surrounding foreground is computed and stored in the *AO average distance field*. In addition, for each voxel the AO eigenvalues of the covariance matrix of the ray intersection points with the foreground are calculated, whereby each AO eigenvalue is stored in a separate scalar field called *AO eigenvalue fields 1, 2,* and *3*. For rays that do not intersect with the foreground, the previously defined ray length is used to compute pseudo-intersection points. Notice, that the number of emitted rays influences the level of detail of the produced results. Furthermore, the predefined length of the rays influences and allows optimisation of the resulting segmentation; different ray lengths allow to focus on different structures. However, both factors as well as the number of selected AO-derived values highly influence the demand on computer resources and computing time, and should, therefore, be considered with care. To further improve the quality of the results produced by the AO algorithm, we herein implemented the option of a per-voxel rotation of the emitted rays and a subsequent moving average window of variable size.

3. Material and methods

The complex workflow of the presented study, including the CT data acquisition (Sect. 3.1.), cavity segmentation (Sect. 3.2.) and cavity and skeleton separation and classification (Sect. 3.3.) is illustrated in Figure 2.

3.1. CT data acquisition

3.1.1. Bryozoan specimen

The bryozoan (moss animal) *Cellaria bafouri* Matsuyama, Titschack, Baum & Freiwald, 2015 was collected during RV Maria S. Merian cruise MSM 16/3 off Mauritania (station GeoB14760-2, 19°44.292′N, 17°08.754′W, 478 m; Matsuyama *et al.*, 2015; Westphal *et al.*,

2012). Prior to the micro-CT scan, the specimen was macerated in household bleach and cleaned in an ultrasonic bath. The scan was performed at Senckenberg am Meer, Wilhelmshaven, Germany, with a Skyscan (now Bruker) micro-CT for Scanning Electron Microscopes (SEM) attached to a Tescan VEGA3 XMU SEM. Raw data were reconstructed using NRecon ver. 1.6.3.3 (Skyscan) software with a voxel size of 3.97 µm (xyz-dimension: 512 × 601 × 566 voxel). A Gaussian smoothing filter with a standard deviation of 2.5 was used for noise reduction.

3.1.2. Ophiuroid tooth

The investigated ophiuroid (brittle star) tooth was extracted from a specimen of *Amphiura filiformis* (Müller, 1776), which was collected south-east off the island of Helgoland, German Bight (North Sea, 54°7.5′N, 07°57.0′E) in April 2014 at 38 m depth with the RV *Aade*. The specimen was fixed in ethanol. Subsequently, the jaws were carefully cut from the body disc and macerated in household bleach. The teeth were sorted, rinsed and air-dried prior to the micro-CT scanning. The tooth was scanned at beamline 2-BM (A) of the Advanced Photon Source, Argonne National Laboratory using 25 keV x-radiation. Projections were recorded every 0.12° over 180°, and the stack of slices were reconstructed with a voxel size of 1.45 µm (xyz-dimension: 168 × 123 × 223 voxel; for further details see Wang *et al.*, 2001). The non-local means filter (in 2D-mode) of Amira ZIB edition (version 2015.31) was applied on the reconstructed volume datasets for noise reduction.

3.1.3. Bioeroded marble block

The bioeroded marble block originates from a settlement experiment carried out at the island of Rhodes (Greece; Bromley *et al.*, 1990) and studied in detail by Färber *et al.* (2016). The presently selected marble block had been placed in 3 m water depth for seven years off Kolymbia (east coast of Rhodes). The bioerosion traces constitute predominantly of millimetre-sized cavities excavated by boring sponges. The scan was performed at the Bundesanstalt für Materialforschung und -prüfung (BAM), Berlin, Germany, with the BAM 225 kV micro-CT system (X-ray source voltage: 210 kV, current: 90 µA, pre-filter: 1 mm copper, 2400 projections over 360°; measurement time: 16 h; Badde and Illerhaus, 2008). Images were reconstructed using BAM software generated from the original “Feldkamp” algorithm (Feldkamp *et al.*, 1984) with a voxel size of 72 µm (xyz-dimension: 1528 × 1501 × 425 voxel). The non-local means filter (in 2D-mode) of the Amira ZIB edition (version 2015.31) was applied on the reconstructed volume datasets for noise reduction.

3.1.4. Coral specimen

The specimen of *Dendrophyllia* sp. was collected with MARUM *ROV Cherokee* from the SSE slope of El Idrissi Bank (central Alboran Sea, Mediterranean Sea) in a water depth of 488 m (GeoB13717-1, sample 6; 36°05.67′N, 03°31.98′E) during RV POSEIDON cruise POS385 in the year 2009 (Hebbeln *et al.*, 2009). Besides its calice (central cavity in which the polyp lives), the species exhibits a complex porous theka (outer wall of the corallite). The specimen was scanned in two partial scans with the micro-CT ProCon CT-ALPHA of the *Petrology of the Ocean Crust* research group, Department of Geosciences, University of Bremen, Germany, with a beam energy of 100 kV, an energy flux of 300 µA, a thin copper filter and a 360° scan rotation with a step size of 0.3°. Raw data was reconstructed with Fraunhofer software VOLEX ver. 6.0, using a GPU-hosted modified Feldkamp algorithm based on filtered backprojection (Feldkamp *et al.*, 1984). The scans have a voxel size of 12.04 µm and the xyz-dimension of the fused dataset is 1347 × 1378 × 3300 voxels. The Avizo 9 bilateral filter (in 3D-mode with a voxel window of 5) was applied to reduce noise within the reconstructed volume datasets. Subsequently, the two partial scans were merged in Amira ZIB edition (version 2015.31).

3.2. Cavity segmentation

CT data processing was performed with the Amira ZIB edition software version 2016.33 (Stalling *et al.*, 2005; http://amira.zib.de). The cavity segmentation, performed on the bryozoan, the marble block and the dendrophyllid coral, consists of three steps (Figs. 1D-G, 2): (i) threshold segmentation of the organism skeletons and marble with the *SegmentationEditor* (not performed on the ophiuroid tooth); (ii) running the *AmbientOcclusionField* module on the background label (‘material’ within Amira) containing the air within the object and the object-surrounding space (number of rays: 156; ray length: ranging from 1 to 0.2 mm for the bryozoan specimen and exceeding the cavity diameter in all other specimens). Thereby, the *AmbientOcclusionField* module was run in two specifications (Fig. 2). First with the specifications of Baum and Titschack (2016), and second with the herein implemented improvements by a random per-voxel rotation of the emitted rays (100 random rotations) combined with a smoothing filter (5 × 5 × 5 voxel moving window averaging filter). The resulting AO fields comprised normalised values ranging between 0 (not occluded at all) and 1 (fully occluded; Fig. 1F). By using a ray length that exceeded the diameter of the specimen, it was ensured that all voxels that were not directly visible from the outside gained an AO value of 1. Voxels visible from the outside and close to the objects surface gained AO values <1 depending on their openness to the surrounding space. With increasing distance from the object

surface, the AO values decreased to 0 when the distance from the specimen surfaces exceeded the ray length (Fig. 1F). In addition to the AO field itself, the AO average distance field and the AO eigenvalue fields 1-3 (AO-derived fields) were calculated. The data range of the latter scalar fields depends highly on the previously defined ray length. As last step (iii), threshold segmentations of the cavity space were carried out within the *SegmentationEditor* on the AO field and AO-derived fields.

3.3. Cavity and skeleton separation and classification

For the separation and classification of specific cavity and skeletal structures, an additional segmentation was performed on the previously segmented label of interest, here the zooid cavities of the bryozoan, the stereom of the ophiuroid tooth, the bioerosion cavities within the marble block, and the calice and theca pore network within the dendrophyllid coral (Fig. 2). The used segmentations of the labels of interest were based on a marker-based watershed segmentation (markers were obtained by threshold segmentation) of the CT-data in case of the ophiuroid tooth and on threshold segmentations of the AO fields calculated with the improved AO algorithm (threshold: 0.7) for all other cases. Subsequently, the labels were cleaned from artefacts (false segmentations on the object surface were removed) and the improved *AmbientOcclusionField* (same specification as mentioned above) and the *DistanceMap* module were run on the respective label of interest. All subsequent segmentations were performed on all AO-derived fields (AO average distance, AO eigenvalues 1 - 3). The obtained results were compared with segmentations that were based on a distance map (scalar) field (Jones et al., 2006; Rosenfeld and Pfaltz, 1966) – a field commonly used for such type of segmentation problem (Ghalib and Hryciw, 1999; Homberg et al., 2012; Malpica et al., 1997; Oberlaender et al., 2009). Note that the distance map stores for each voxel the closest distance to the foreground while the AO average distance field averages over many distances.

Zooid separation within the investigated bryozoan specimen was obtained with the *ContourTreeSegmentation* module (threshold: -0.09, persistence value: 0.0002 - 0.00005 for all AO-derived fields; threshold: 0, persistence value: 0.02 for the distance-map field). The *ContourTreeSegmentation* module was also used for the boring-trace separation within the bioeroded marble block (threshold: -0.09; persistence value: 1.5 for the AO-derived fields; threshold: 0; persistence value: 1 for the distance-map field). The structures with varying thickness within the ophiuroid tooth stereom were segmented using the threshold segmentation within the *SegmentationEditor*. Thresholds had to be optimised separately for the AO-field- and AO-derived-field-based segmentations. The separation of the pore network in the corallite

walls and the calice within the dendrophyllid coral was obtained with the marker-based *WatershedSegmentation* module. Special care had to be taken during the threshold segmentation of the markers with the *SegmentationEditor* to obtain satisfying segmentation results – often several iterations of marker optimisation were needed.

4. Results

4.1. Cavity segmentation

The cavity segmentation was performed on the AO and AO-derived fields and two aspects were evaluated: (i) the improvement of cavity segmentation by the incorporation of a random per-voxel ray rotation combined with a smoothing filter (moving-window averaging filter) compared to the original AO algorithm published by Baum and Titschack (2016; Sect. 4.1.1.); and (ii) the quality of cavity segmentation as subject to the ray length (Sect. 4.1.2.). Those tests were exclusively performed on the bryozoan specimen due to the fact that this specimen exhibits a high cavity opening complexity accompanied with a complex outer surface morphology.

4.1.1. Cavity segmentation using the AO algorithm with and without rotating rays and subsequently applied smoothing filter

The herein introduced improvements of the AO algorithm were evaluated by comparing the segmentation results produced with the original AO algorithm (Baum and Titschack, 2016; Figs. 3 - 7 upper row), with those of the improved AO algorithm (Figs. 3 - 7 lower row) using the same input and threshold parameters. The cavity-surrounding space boundary always exhibits a concave shape. The visual comparison of the cavity segmentation based on the AO and all AO-derived fields revealed that the best segmentation was obtained with the AO field itself (1 mm ray length). For cavity segmentations that relied on the AO-derived fields (Figs. 4 - 7), only the segmentation based on the AO average distance (Fig. 4) and AO eigenvalue 2 fields (both with 1 mm ray length; Fig. 6) showed satisfying results with only a slight increase of artefacts (areas segmented on the object surface that were not connected to a cavity).

The comparison between the cavity segmentation results of the original and the improved AO algorithm revealed a better performance of the improved AO algorithm for all ray lengths, shown by a considerable visual reduction of artefacts (Figs. 3 - 7). The reduction of artefacts by the application of the improved AO algorithm is also reflected in the calculated cavity

volumes. The cavity volumes of the improved AO-algorithm-based segmentations is always smaller than the cavity volumes obtained from the original AO-algorithm-based segmentations. This is interpreted to reflect the reduction of artefacts on the object surface (only comparing volumes calculated with the same ray length; Fig. 8). A potential change in curvature of the cavity-surrounding-space boundary as reason for the observed volume reduction can be excluded due to the fact that the degree of curvature is predominantly controlled by the ray length as is clearly visible in Figures 3 – 7, right column.

4.1.2. Dependence of the ambient occlusion ray length on the segmentation

The influence of the ray length on the segmentation result was investigated by running the AO algorithm with ray lengths of 1 mm, 0.4 mm and 0.2 mm. While the 1 mm ray length exceeded the maximum cavity diameter by nearly a factor of 2, the minimum ray length of 0.2 mm was close to the shortest cavity diameter. Furthermore, the effect of the input scalar field (AO field, AO average distance field, AO eigenvalue 1 – 3 fields; Figs. 3 - 7) was examined for the final segmentation.

The results revealed that the segmentations based on the AO fields (i) showed the lowest degree of artefacts on the skeleton surface (Figs. 3 - 7); (ii) exhibited the lowest inward dislocation of the cavity-surrounding-space boundary with decreasing ray length (Figs. 3 - 7, right column); (iii) showed the lowest spread in the volume of the segmented cavities over the entire range of ray lengths (Fig. 8); and (iv) presented the only segmentations that could be performed with one consistent threshold (0.7; Fig. 3). All segmentations based on the AO-derived fields revealed a strong dependence on the ray length and needed a ray-length-dependent threshold optimisation (Figs. 4 - 7). The comparison of all results revealed that the best segmentations were always obtained with scalar fields calculated with a ray length of 1 mm (Figs. 3 - 8).

4.2. Cavity separation and stereom classification

For the investigation of the cavity and stereom structure of the investigated specimens, the AO algorithm was applied to the previously segmented object of interest (cavities in case of the bryozoan, coral and marble block; tooth stereom in case of the ophiuroid) with a ray length exceeding the length of the respective specimen (for the detailed workflow see Fig. 2). The subsequent separation/classification of the cavities and tooth stereom were tested on the AO average distance field and the AO eigenvalue 1 - 3 fields. The obtained results were compared with a segmentation based on a distance map field of the respective object of interest.

4.2.1. Zooid separation within the bryozoan

The zooid segmentation within the bryozoan *Cellaria bafouri* specimen, achieved by a *ContourTreeSegmentation*, provided a good automatic separation of the zooids from each other for all segmentations (Fig. 9 A1 - A5). Only minor misclassifications were observed (see circles in Fig. 9 A2 - A5). However, the best segmentation with 21 identified zooids and well-located zooid boundaries were obtained with the distance map field (Fig. 9 A1). All AO-derived-field-based segmentations provided clearly too many segmented zooids (between 34 and 41). Furthermore, the zooid boundaries were partially incorrect and some zooids were horizontally split into two (see circles in Fig. 9 A2 - A5).

4.2.2. Classification of the ophiuroid tooth stereom

The variations in thickness within the tooth stereom of the ophiuroid *Amphiura filiformis* were classified by threshold segmentation. All AO-derived fields provided a good visualisation of the variations in thickness within the tooth stereom (i.e., thick stereom elements and narrow stromal space) as well as good separation of areas with thick, moderate and thin tooth stereom (Fig. 9 B2 - B5). However, for every AO-derived field, the thresholds had to be re-optimised. With the distance map field, no satisfying segmentation could be achieved by thresholding (Fig. 9 B1) or other segmentation algorithms. Only the area with the thickest tooth stereom could be visualised, but not segmented into a separate label.

The obtained results for the AO-derived fields led to the observation that (i) the tooth, apart from its previously known thickly calcified cap at the distal end, revealed two additional thickly calcified stereom areas at the base of the tooth; and (ii) the thinly calcified stereom area is predominantly located in the central part of the tooth (Fig. 9 B2 - B5).

4.2.3. Separation of bioerosion traces within the marble block

For the separation of various bioerosion traces within the investigated marble block (Fig. 9 C1 - C5) the *ContourTreeSegmentation* was used. All obtained segmentations revealed a good separation of individual traces, which were dominated by sponge borings (*Entobia* ispp.; Fig. 9 C1 - C5). However, the segmentations based on the distance map field (Fig. 9 C1) and AO eigenvalue 3 (Fig. 9 C5) showed a separation of consistent boring in the upper left corner of the investigated sample (upper circle) and a lacking differentiation of two distinctively different borings in the lower left corner (lower ellipse). Segmentations based on AO eigenvalues 1 (Fig. 9 C3) and 2 (Fig. 9 C4) separated the borings in the lower left corner but also the consistent boring in the upper left corner. Only the AO average distance field-based segmentation

provided a good segmentation of the boring in the upper left corner and separation of different borings in the lower left corner (Fig. 9 C2).

4.2.4. Calice-pore separation within the dendrophyllid coral

The separation of the marginal pore system from the calice (corallite cavity) within the investigated coral *Dendrophyllia* sp. specimen was achieved using a marker-based watershed segmentation. Here, the segmentation of the markers was a crucial step that had a major influence on the final segmentation. The segmentation of markers was easily achieved by *threshold* segmentation from the AO average distance and the AO eigenvalue 1 and 2 fields and only minor manual post-processing was needed to obtain markers for a good calice-pore separation from the respective data field (Fig. 9 D2 - D4). The segmentation of markers from the AO eigenvalue 3 field was time consuming and the respective segmentation presented multiple artefacts dominated by intra-calice space classified as marginal pore space (Fig. 9 D5). The segmentation of the markers from the distance map field allowed a very good segmentation of the calice markers but failed by when segmenting the pore markers. Using markers obtained from the AO average distance field for the distance-map-based calice-pore separation resulted in an unreliable separation (Fig. 9 D1). The best segmentation was achieved by running the marker-based watershed segmentation on the AO average distance field (Fig. 9 D2).

5. Discussion

5.1. Cavity segmentation

First CT studies concentrating on cavity/skeletal structures date back to the mid-1990s (e.g., Kinney *et al.*, 1993) and include the 3D visualisation (e.g., Beuck *et al.*, 2007, 2008; Riley *et al.*, 2014) and quantification of cavities (e.g., Homberg *et al.*, 2012; Knackstedt *et al.*, 2008; Soete *et al.*, 2015; Werth *et al.*, 2010; Zong *et al.*, 2014). Wherever cavity structures are connected to the object surface, the separation of the space within the object from the object-surrounding space, both commonly consisting of air after sample preparation, is crucial (Kline and Ritman, 2012). For objects, for which the relationship between the object surface and the exterior cavity surface is not relevant, such as rock plugs or field rock samples, the object can just be cropped so that no object surrounding space is left (e.g. Luo *et al.*, 2010; Peth *et al.*, 2008). However, depending on the complexity of the object surface, the cropping procedure might cause tremendous loss of data, which unnecessarily increases potential analytical uncertainties. For objects, for which the relationship between the object surface and the exterior

cavity surface is relevant, such as for shells and skeletons, the separation of the cavity space within the object from the object-surrounding space is important and currently difficult to obtain. Hence, a fast and reproducible segmentation of the cavity space allows (i) the reduction of analytical uncertainties in objects, for which the relationship between the object surface and the exterior cavity surface is of no interest, and (ii) the quantitative analysis of objects, for which the relationship between the object surface and the exterior cavity surface is necessary. Due to the fact that the cavity space reveals similar or equal values when compared to the object-surrounding space, threshold segmentation as well as sophisticated segmentation methods, such as watershed- (Malpica *et al.*, 1997), contour-tree- (Carr *et al.*, 2003, 2010; Kass *et al.*, 1988) or discrete-Morse-theory-based segmentation methods (Delgado-Friedrichs *et al.*, 2015; Gyulassy *et al.*, 2014), including distance field approaches (Ghalib and Hryciw, 1999; Jones *et al.*, 2006; Malpica *et al.*, 1997), cannot be successfully applied. Morphological operations are used for the segmentation of cavities but are prone to artefacts, especially for cases where the cavity openings to the object-surrounding space are wider than the cavities themselves and/or exhibit a high morphological variability. Roche *et al.* (2010) and Kline and Ritman (2012) separated the cavity space within coral and sponge skeletons from the specimen-surrounding space by applying shrink-wrap approaches. However, these approaches process the data slice-wise, hence they do not consider the full 3D shape, which might result in orientation-dependent artefacts. In contrast, the approach taken by Baum and Titschack (2016), which uses the AO concept as segmentation algorithm for the separation of the cavity space from the object-surrounding space, exploits the full 3D shape information and is, therefore, orientation-independent. The authors applied this methodology to segment the central cavity (calice) within corallites and to segment the cavity space within a rock sample. Matsuyama *et al.* (2015) and Färber *et al.* (2016) applied the algorithm successfully to segment bryozoan zooids and bioerosion traces within marble blocks, respectively. AO fields (e.g., Fig. 1F) and further AO-derived fields allowed the fast interactive threshold segmentations of the cavity space within the herein studied bryozoan (Figs. 3 - 7). The results clearly highlight that the segmentations based on the AO field provide the best cavity segmentation and are relatively inert to changes of the ray length input parameter (Figs. 3, 8). The segmentation that was based on the herein improved AO algorithm showed minor improvements in the occurrence of visual artefacts on the object surface (Fig. 3), also indicated by the slightly smaller cavity volume (Fig. 8).

Cavity segmentations that were based on the AO-derived fields provided reasonably good results (Figs. 4 - 7). However, the quality of their cavity segmentations depended on several factors: (i) the thresholds had to be optimised separately for every AO-derived field to obtain a

good segmentation (Figs. 4 - 7). (ii) The length of the emitted rays had a strong influence on the number of visual artefacts on the object surface. The number of artefacts increased with decreasing lengths of the emitted rays (Figs. 4 - 7). Additionally, the artefacts led to an increase of the segmented cavity volume, clearly visible when comparing the segmentations based on AO or AO-derived fields calculated with the improved and original AO algorithm (Fig. 8). And (iii) the length of the emitted rays had a strong influence on the inward dislocation of the cavity-surrounding space boundary (Figs. 4 - 7, right column). Decreasing the ray length caused, besides an increase of artefacts, an unrealistic inward dislocation of the cavity-surrounding space boundary. This resulted in a reduction of the segmented cavity volume which, however, outpaced the cavity volume increase resulting from the concurrent increase in artefacts on the object surface (Fig. 8). The best segmentation results were obtained with the AO average distance (1 mm ray length; Fig. 3) and AO eigenvalue 2 fields (0.4 mm ray length; Fig. 6).

The herein introduced implementation of (i) a random per-voxel rotation of the emitted rays and (ii) a smoothing filter that consists of a moving-window averaging filter with freely selectable window sizes, provided improved AO and AO-derived fields with a reduction of artefacts that are caused by very small irregularities on the object surface (Figs. 3 - 7). The user-defined number of random rotations and window size of the averaging filter allow optimising the segmentation and computing time. Cavity segmentations based on AO and AO-derived fields calculated with the herein improved algorithm showed generally reduced volumes compared to original AO algorithm-based segmentations (Fig. 8) that are interpreted to reflect the reduction of visible artefacts on the object surface (Figs. 3 - 7). The concavity of the cavity-surrounding-space boundary was not affected by the improvements of the AO algorithm but depends highly on the emitted ray lengths (Figs. 3 - 7 right column).

5.2. Cavity separation and skeleton classification based on AO-derived fields

AO-derived fields (AO average distance and AO eigenvalue fields) were used for the separation/classification of complex skeletal and cavity structures by various segmentation methods (e.g., threshold, marker-based watershed, and contour-tree segmentation). The chosen segmentation method depended on the desired result and the specific morphological structure of the investigated object.

Baum and Titschack (2016) showed that the AO average-distance-based separation of interconnected calices of multiple corallites within a coral colony is superior to a separation based on a distance-map field. The good characteristics of the AO average-distance field for the separations/classifications of cavities and skeletal structures is confirmed by the herein

presented results that showed separations or classifications which were clearly superior to most distance-map-based segmentations (Fig. 9). AO-derived-field-based segmentations of the ophiuroid tooth stereom, the bioerosion within the marble block and the dendrophyllid coral were superior to distance-map-based segmentations. For the classification of the ophiuroid tooth stereom, the distance-map-based stereom classification even failed (Fig. 9 B1), which is most likely due to the specific spatial information saved within the latter field. For the separation of bioerosion traces within the marble block, a perfect separation of the various sponge borings was not expected because the spatial resolution of 72 µm did not allow the segmentation of all thin exploratory and connecting threads, and due to the presumed overprinting of different generations of sponge borings where younger borings penetrated older ones (Färber *et al.*, 2016). However, all segmentations provided reasonably good results. The best separation result was achieved with the AO average distance field (Fig. 9 C2). All other segmentations lead to the fragmentation of consistent borings and/or joined different borings (Fig. 9 C1, C3 – C5). Within the dendrophyllid coral, all AO-derived field-based pore network/calice separations were better than the distance-map-based segmentation (Fig. 9 D). However, the best segmentation was again achieved with the AO average distance field (Fig. 9 D2). Only for the zooid separation of the bryozoan specimen the distance-map-based segmentation provided the best result with 21 (20 correctly) identified zooids, which is closest to the 24 visually identified zooids by Matsuyama *et al.* (2015). The AO-derived-field-based segmentations provided a total number of >34 zooids and showed partially incorrectly identified zooids (see circles in Figs. 9 A2 - A5).

6. Conclusions

The AO algorithm introduced by Baum and Titschack (2016) provides a promising alternative to, e.g., shrink-wrap approaches for the segmentation of cavities within objects. While the latter approaches only consider 2D slices, the AO algorithm takes into account the full 3D shape information. Its fast application as well as the robustness of the algorithms to variable input parameters and the interactive threshold segmentation provide a high user-friendliness and make this algorithm attractive even to non-specialists. Its application is not restricted to CT data but can be applied to any 3D volume dataset with similar characteristics.

The best cavity segmentation was obtained by using the AO field calculated with a ray length that exceeded the maximum diameter of the cavities and a threshold value of 0.7 that seems to be uniquely applicable. This makes cavity segmentation comparable across many datasets.

The herein presented improved AO algorithm includes a per-voxel random rotation of the emitted rays and a subsequently applied smoothing filter. This implementation results in smoothed AO and AO-derived fields. While the obtained segmentations show only a small reduction of artefacts for AO-field-based segmentations, AO-derived-field-based segmentations improved considerably.

AO-derived fields were successfully used to separate zooids within a bryozoan, to classify an ophiuroid tooth stereom, to separate bioerosion traces within a marble block and to separate the calice from the marginal pore system within a dendrophyllid coral. The obtained results clearly show that a successful separation or classification of cavity and skeletal structures highly depends on the 3D morphology of the investigated object of interest. Different segmentation algorithms must be tested on various input fields (AO-derived or distance-map fields) to obtain an optimal separation/classification/segmentation result. However, the AO average distance field seems to provide the broadest applicability. A combined use of all fields together in a supervised (e.g., random forest, maximum-likelihood) or unsupervised segmentation methods (e.g., clustering) might be a promising future direction to further improve high-end data segmentations. These segmentation methods might even make the optimisation of thresholds unnecessary.

7. Acknowledgements

We thank the crews of the RV Aade (Biologische Anstalt Helgoland, Marine Station of the Alfred Wegener Institute for Polar and Marine Research), RV POSEIDON cruise POS385 and RV Maria S. Merian cruise MSM 16/3 for their help and dedication during the cruises and sampling. André Freiwald (Senckenberg am Meer, Wilhelmshaven, Germany) is gratefully acknowledged for providing the dendrophyllid coral specimen and Agostina Vertino for confirming its taxonomy. KB and JT received funding from GLOMAR – Bremen International Graduate School for Marine Sciences, KM from the Hessian initiative for the development of scientific and economic excellence (LOEWE) at the Biodiversity and Climate Research Centre (BiK-F), Frankfurt, Germany. CF received funds by the Deutsche Forschungsgemeinschaft (Grant Wi 3754/2-1). SRS acknowledges support from US NICDR grant DE001374, and use of the Advanced Photon Source was supported by the US Department of Energy, Office of Science, Office of Basic Energy Sciences, under Contract No. DE-AC02-06CH11357. We greatly appreciate the thourough review provided by Bernhard Ruthensteiner, which considerably helped to improve the manuscript.

8. References

Badde, A., Illerhaus, B., 2008. Three dimensional computerized microtomography in the analysis of sculpture. Scanning 30, 16-26.

Baum, D., Titschack, J., 2016. Cavity and pore segmentation in 3D images with ambient occlusion, In: Bertini, E., Elmqvist, N., Wischgoll, T. (Eds.), Eurographics Conference on Visualization (EuroVis) 2016. The Eurographics Association, pp. 113-117.

Beuck, L., Vertino, A., Stepina, E., Karolczak, M., Pfannkuche, O., 2007. Skeletal response of *Lophelia pertusa* (Scleractinia) to bioeroding sponge infestation visualised with micro-computed tomography. Facies 53, 157-176.

Beuck, L., Wisshak, M., Munnecke, A., Freiwald, A., 2008. A giant boring in a Silurian stromatoporoid analysed by computer tomography. Acta Palaeontologica Polonica 53, 149-160.

Borland, D., 2011. Ambient occlusion opacity mapping for visualization of internal molecular structure. Journal of WSCG 1-3, 17-24.

Bromley, R.G., Hanken, N.-M., Asgaard, U., 1990. Shallow marine bioerosion: preliminary results of an experimental study. Bulletin of the Geological Society of Denmark 38, 85-99.

Carr, H., Snoeyink, J., Axen, U., 2003. Computing contour trees in all dimensions. Computational Geometry 24, 75-94.

Carr, H., Snoeyink, J., van de Panne, M., 2010. Flexible isosurfaces: Simplifying and displaying scalar topology using the contour tree. Computational Geometry 43, 42-58.

Cnudde, V., Masschaele, B., Dierick, M., Vlassenbroeck, J., Hoorebeke, L.V., Jacobs, P., 2006. Recent progress in X-ray CT as a geosciences tool. Applied Geochemistry 21, 826-832.

Correa, C., Kwan-Liu, M., 2009. The occlusion spectrum for volume classification and visualization. Visualization and Computer Graphics, IEEE Transactions on 15, 1465-1472.

Dachsbacher, C., Stamminger, M., Drettakis, G., Durand, F., 2007. Implicit visibility and antiradiance for interactive global illumination. ACM Transactions on Graphics 26, 61.

Delgado-Friedrichs, O., Robins, V., Sheppard, A., 2015. Skeletonization and partitioning of digital images using discrete Morse theory. IEEE Transactions on Pattern Analysis and Machine Intelligence 37, 654-666.

Eicken, H., Bock, C., Wittig, R., Miller, H. and Poertner, H.O., 2000. Magnetic resonance imaging of sea-ice pore fluids: methods and thermal evolution of pore microstructure. Cold Regions Science and Technology 31, 207-225

Färber, C., Titschack, J., Schönberg, C.H.L., Ehrig, K., Boos, K., Baum, D., Illerhaus, B., Asgaard, U., Bromley, R.G., Freiwald, A., Wisshak, M., 2016. Long-term macrobioerosion in the Mediterranean Sea assessed by micro-computed tomography. Biogeosciences 13, 3461-3474.

Feldkamp, L.A., Davis, L.C., Kress, J.W., 1984. Practical cone-beam algorithm. Journal of the Optical Society of America A 1, 612-619.

Fredrich, J.T., 1999. 3D imaging of porous media using laser scanning confocal microscopy with application to microscale transport processes. Physics and Chemistry of the Earth, Part A: Solid Earth and Geodesy 24, 551-561.

Ghalib, A.M., Hryciw, R.D., 1999. Soil particle size distribution by mosaic imaging and watershed analysis. Journal of Computing in Civil Engineering 13, 80-87.

Gyulassy, A., Günther, D., Levine, J.A., Tierny, J., Pascucci, V., 2014. Conforming Morse-smale complexes. IEEE Transactions on Visualization and Computer Graphics 20, 2595-2603.

Hebbeln, D., Wienberg, C., Beuck, L., Freiwald, A., Wintersteller, P., cruise participants, 2009. Report and preliminary results of RV POSEIDON Cruise POS 385 "Cold-Water

Corals of the Alboran Sea (western Mediterranean Sea)", Faro - Toulon, May 29 - June 16 2009, Reports of the Department of Geosciences (GeoB), University of Bremen, p. 79.
Homberg, U., Baum, D., Prohaska, S., Kalbe, U., Witt, K., 2012. Automatic extraction and analysis of realistic pore structures from mCT data for pore space characterization of graded soil, Proceedings of the 6th International Conference on Scour and Erosion (ICSE-6), pp. 66-73.
Jones, M.W., Baerentzen, J.A., Sramek, M., 2006. 3D distance fields: a survey of techniques and applications. IEEE Transactions on Visualization and Computer Graphics 12, 581-599.
Kass, M., Witkin, A., Terzopoulos, D., 1988. Snakes: Active contour models. International Journal of Computer Vision 1, 321-331.
Kinney, J.H., Breunig, T.M., Starr, T.L., Haupt, D., Nichols, M.C., Stock, S.R., Butts, M.D., Saroyan, R.A., 1993. X-ray tomographic study of chemical vapor infiltration processing of ceramic composites. Science 260, 789-792.
Kline, T.L., Ritman, E.L., 2012. Characterization of the pore labyrinth geometry of sea sponges imaged by micro-CT. Journal of Porous Materials 19, 141-151.
Knackstedt, M.A., Sok, R.M., Sheppard, A.P., Latham, S.J., Madadi, M., Varslot, T., Arns, C.H., Bachle, G., Eberli, G., 2008. Probing Pore Systems In Carbonates: Correlations to Petrophysical Properties. Society of Petrophysicists and Well-Log Analysts.
Landis, H., 2002. Production ready global illumination, In Siggraph 2002 Course Notes, pp. 331–338.
Long, H., Swennen, R., Foubert, A., Dierick, M., Jacobs, P., 2009. 3D quantification of mineral components and porosity distribution in Westphalian C sandstone by microfocus X-ray computed tomography. Sedimentary Geology 220, 116-125.
Loos, B.J., Sloan, P.-P., 2010. Volumetric obscurance, I3D '10: Proceedings of the 2010 ACM SIGGRAPH symposium on Interactive 3D Graphics and Games. ACM, Washington, D.C., pp. 151-156.
Luo, L., Lin, H., Li, S., 2010. Quantification of 3-D soil macropore networks in different soil types and land uses using computed tomography. Journal of Hydrology 393, 53-64.
Malpica, N., Ortiz de Solórzano, C., Vaquero, J.J., Santos, A., Vallcorba, I., Garcia-Sagredo, J.M., Del Pozo, F., 1997. Applying watershed algorithms to the segmentation of clustered nuclei. Cytometry 28, 289-297.
Matsuyama, K., Titschack, J., Baum, D., Freiwald, A., 2015. Two new species of erect Bryozoa (Gymnolaemata: Cheilostomata) and the application of non-destructive imaging methods for quantitative taxonomy. Zootaxa 4020, 081-100.
Mees, F., Swennen, R., Geet, M.V., Jacobs, P., 2003. Applications of X-ray computed tomography in the geosciences. Geological Society, London, Special Publications 215, 1-6.
Morales Pinzón, A., Orkisz, M., Rodríguez Useche, C.M., Torres González, J.S., Teillaud, S., Sánchez, J.A., Hernández Hoyos, M., 2014. A Semi-Automatic Method to Extract Canal Pathways in 3D Micro-CT Images of Octocorals. PLoS ONE 9, e85557.
Oberlaender, M., Dercksen, V.J., Egger, R., Gensel, M., Sakmann, B. and Hege, H.C., 2009. Automated three-dimensional detection and counting of neuron somata. Journal of Neuroscience Methods 180, 147-160.
Penner, E., Mitchell, R., 2008. Isosurface ambient occlusion and soft shadows with filterable occlusion maps, Proceedings of the Fifth Eurographics / IEEE VGTC conference on Point-Based Graphics. Eurographics Association, Los Angeles, CA, pp. 57-64.
Peth, S., Horn, R., Beckmann, F., Donath, T., Fischer, J., Smucker, A.J.M., 2008. Three-dimensional quantification of intra-aggregate pore-space features using synchrotron-radiation-based microtomography. Soil Science Society of America Journal 72.
Riley, A., Sturrock, C.J., Mooney, S.J., Luck, M.R., 2014. Quantification of eggshell microstructure using X-ray micro computed tomography. British Poultry Science 55, 311-320.

Roche, R.C., Abel, R.A., Johnson, K.G., Perry, C.T., 2010. Quantification of porosity in *Acropora pulchra* (Brook 1891) using X-ray micro-computed tomography techniques. Journal of Experimental Marine Biology and Ecology 396, 1-9.

Rosenfeld, A. and Pfaltz, J.L., 1966. Sequential operations in digital picture processing. Journal of the Association for Computing Machinery (JACM) 13, 471-494.

Sentoku, A., Morisaki, H., Masumoto, S., Ohno, R., Tomiyama, T., Ezaki, Y., 2015. Internal skeletal analysis of the colonial azooxanthellate scleractinian *Dendrophyllia cribrosa* using microfocus X-ray CT images: Underlying basis for its rigid and highly adaptive colony structure. Journal of Structural Biology 189, 37-43.

Soete, J., Kleipool, L.M., Claes, H., Claes, S., Hamaekers, H., Kele, S., Özkul, M., Foubert, A., Reijmer, J.J.G., Swennen, R., 2015. Acoustic properties in travertines and their relation to porosity and pore types. Marine and Petroleum Geology 59, 320-335.

Stalling, D., Westerhoff, M., Hege, H.-C., 2005. 38 - Amira: A Highly Interactive System for Visual Data Analysis, In: Hansen, C.D., Johnson, C.R. (Eds.), Visualization Handbook. Butterworth-Heinemann, Burlington, pp. 749-767.

Stock, S.R., 2008a. MicroComputed Tomography - Methodology and Application. CRC Press, Boca Raton, Fl, USA, 336 pp.

Stock, S.R., 2008b. Recent advances in X-ray microtomography applied to materials. International Materials Reviews 53, 129-181.

Taina, I.A., Heck, R.J., Elliot, T.R., 2008. Application of X-ray computed tomography to soil science: A literature review. Canadian Journal of Soil Science 88, 1-19.

Tarini, M., Cignoni, P., Montani, C., 2006. Ambient Occlusion and Edge Cueing for Enhancing Real Time Molecular Visualization. Visualization and Computer Graphics, IEEE Transactions on 12, 1237-1244.

Wang, Y., De Carlo, F., Mancini, D.C., McNulty, I., Tieman, B., Bresnahan, J., Foster, I., Insley, J., Lane, P., von Laszewski, G., Kesselman, C., Su, M.-H., Thiebaux, M., 2001. A high-throughput x-ray microtomography system at the Advanced Photon Source. Review of Scientific Instruments 72, 2062-2068.

Werth, C.J., Zhang, C., Brusseau, M.L., Oostrom, M., Baumann, T., 2010. A review of non-invasive imaging methods and applications in contaminant hydrogeology research. Journal of Contaminant Hydrology 113, 1-24.

Westphal, H., Beuck, L., Braun, S., Freiwald, A., Hanebuth, T., Hetzinger, S., Klicpera, A., Kudrass, H., Lantzsch, H., Lundälv, T., Vicens, G.M., Preto, N., v Reumont, J., Schilling, S., Taviani, M., Wienberg, C., 2012. Phaeton - Paleoceanographic and paleo-climatic record on the Mauritanian Shelf – Cruise No. MSM16/3 - October 13 – November 20, 2010 - Bremerhaven (Germany) – Mindelo (Cap Verde), MARIA S. MERIAN-Berichte, p. 57.

Zhukov, S., Inoes, A., Kronin, G., 1998. An ambient light illumination model, In: Drettakis, G., Max, N. (Eds.), Rendering Techniques ’98, Eurographics. Springer, Wien, pp. 45-56.

Zong, Y., Yu, X., Zhu, M., Lu, S., 2014. Characterizing soil pore structure using nitrogen adsorption, mercury intrusion porosimetry, and synchrotron-radiation-based X-ray computed microtomography techniques. Journal of Soils and Sediments 15, 302-312.

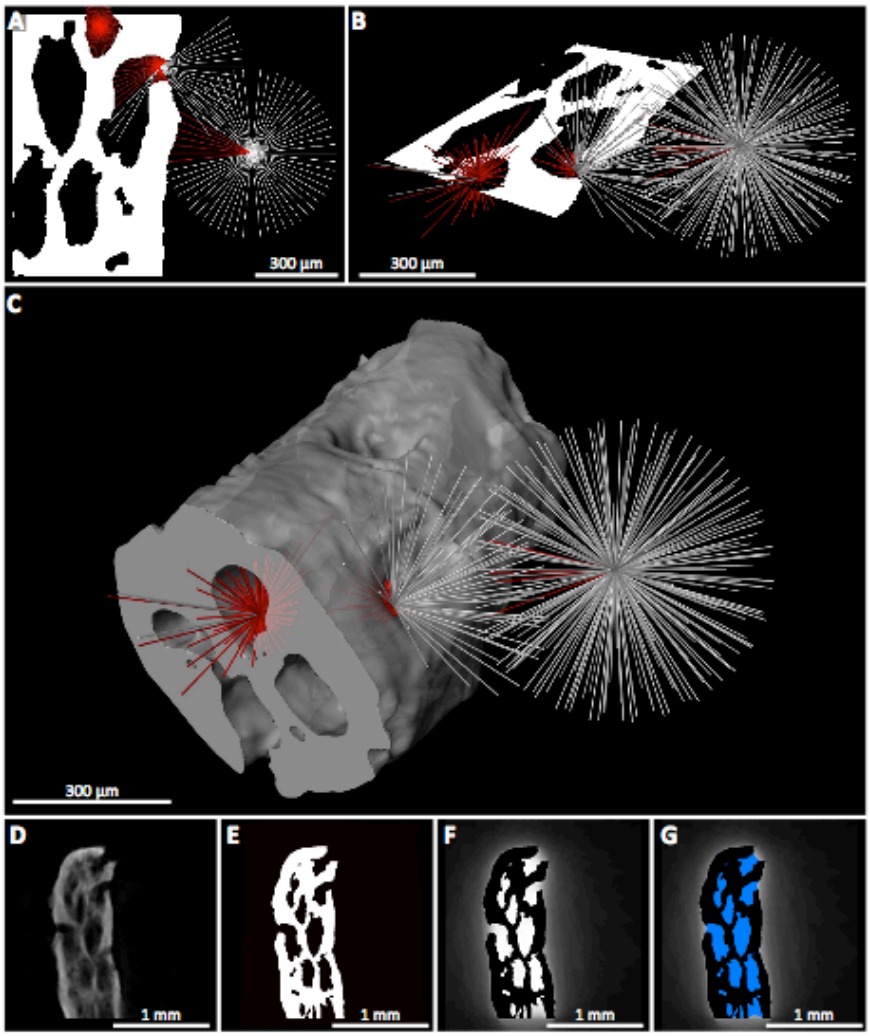

Figure 1. Principle of the ambient occlusion as segmentation algorithm (illustrated for three voxels) exemplified on a bryozoan colony fragment of *Cellaria bafouri*. Top and bottom in A and B as well as the front and back in C are virtually cut for better understanding. The ambient occlusion algorithm emits a predefined number of rays with a predefined length isotropically in all directions from every voxel within the background (black; represented by the air-filled pore/cavity space and surrounding space) and counts the amount of rays that touch or penetrate the foreground (white; in this case a bryozoan skeleton). The ratio between the touching/penetrating rays and all rays is written into the voxel from which the rays were emitted. For the illustrated voxel the ambient occlusion values are from left to right 0.98, 0.76 and 0.03. Derived values of the ambient occlusion principle are, for example, the AO average distance (mean length of rays) or the AO eigenvalues of the covariance matrix of the intersection points. **A**: Two-dimensional view. **B**: Three-dimensional view with the foreground only visualised in one plane. **C**: Three-dimensional view with the foreground shown by slightly transparent surface. **D**: Orthoslice of the original scan. **E**: Threshold segmentation result of the skeleton (foreground). **F**: Ambient occlusion scalar field of the background. **G**: Threshold segmentation of the bryozoan zooids based on the ambient occlusion field (threshold 0.7).

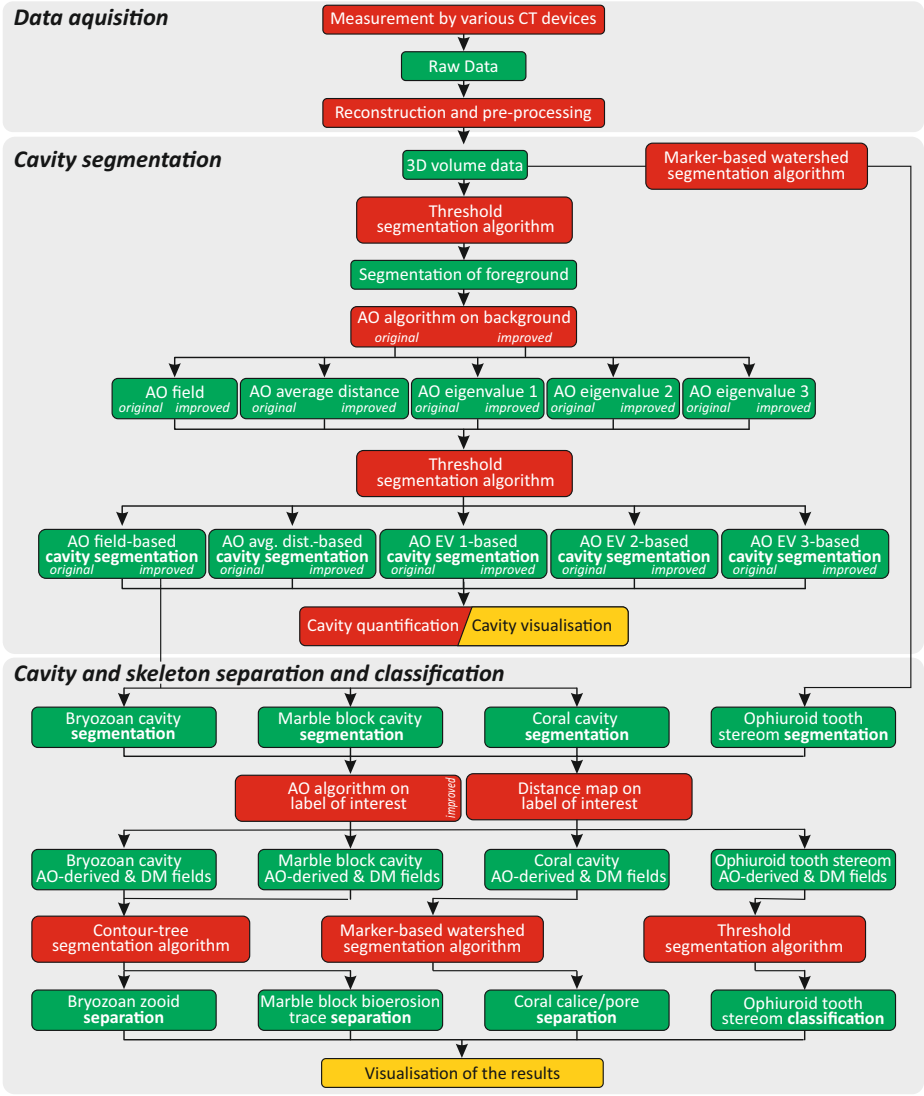

Figure 2. Diagram of the processing workflow from the data acquisition (Sect. 3.1.) to cavity segmentation (Sects. 3.2., 4.1., 5.1.) and separation (Sects. 3.3., 4.2., 5.2.). Algorithms and measurements are indicated in red, datasets in green and visualisations in yellow analogue to the colour labelling within Amira. Avg. dist.: average distance; EV: eigenvalue.

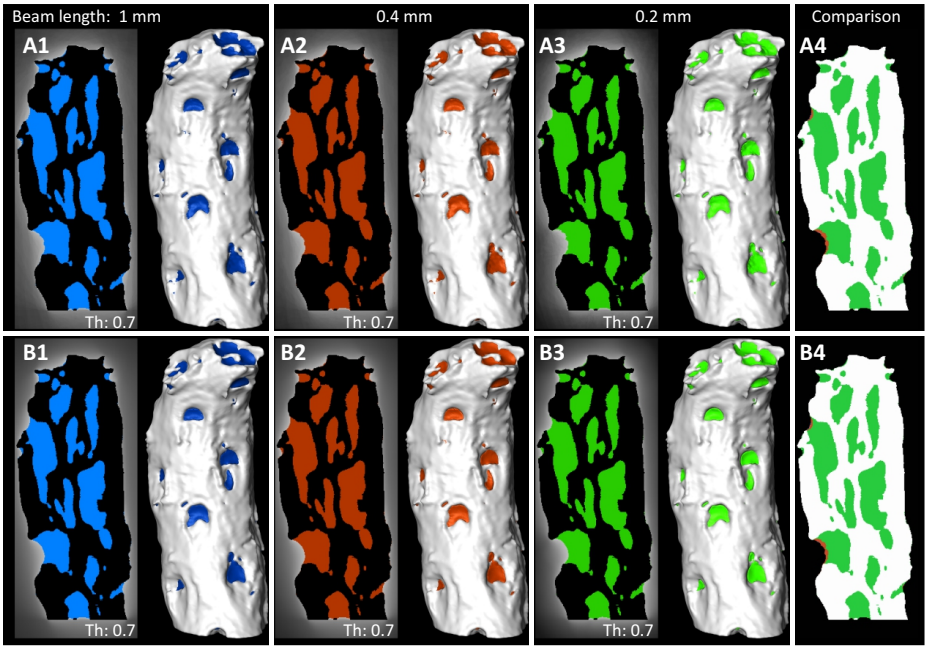

Figure 3. Comparison of the threshold (Th) segmentation based on the ambient occlusion field calculated with the original ambient occlusion algorithm (A1 - A3; Baum and Titschack, 2016) and the improved ambient occlusion algorithm introduced herein (B1 - B3) including the influence of the ray length on the segmentation result. The differences are illustrated in A4 and B4 using the color-coding A1 - A3 and B1 - B3, respectively.

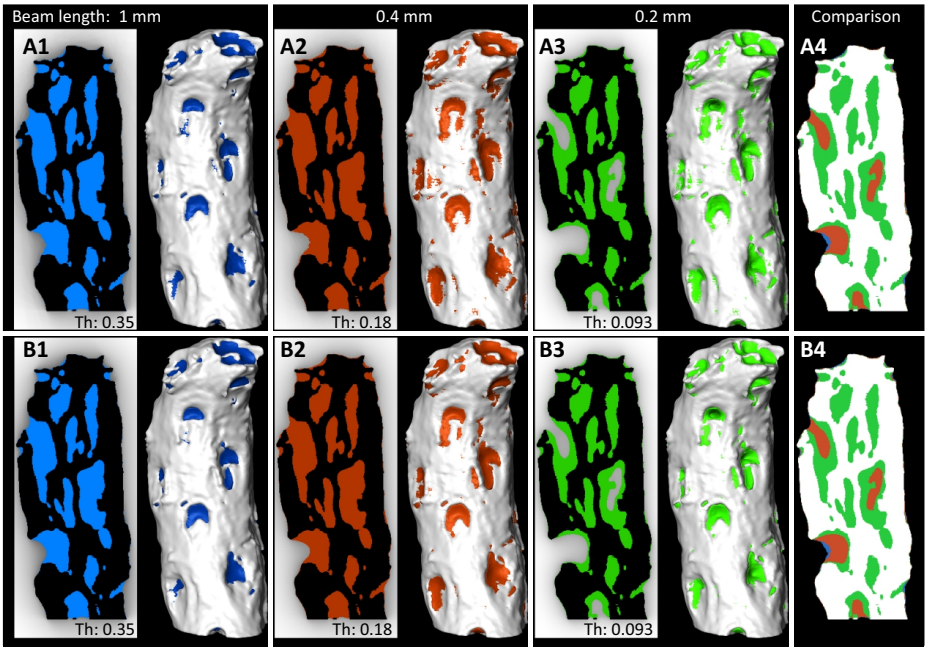

Figure 4. Comparison of the threshold (Th) segmentation based on the ambient occlusion average distance field calculated with the original ambient occlusion algorithm (A1 - A3; Baum and Titschack, 2016) and the improved ambient occlusion algorithm introduced herein (B1 - B3) including the influence of the ray length on the segmentation result. For colour-coding see Figure 3.

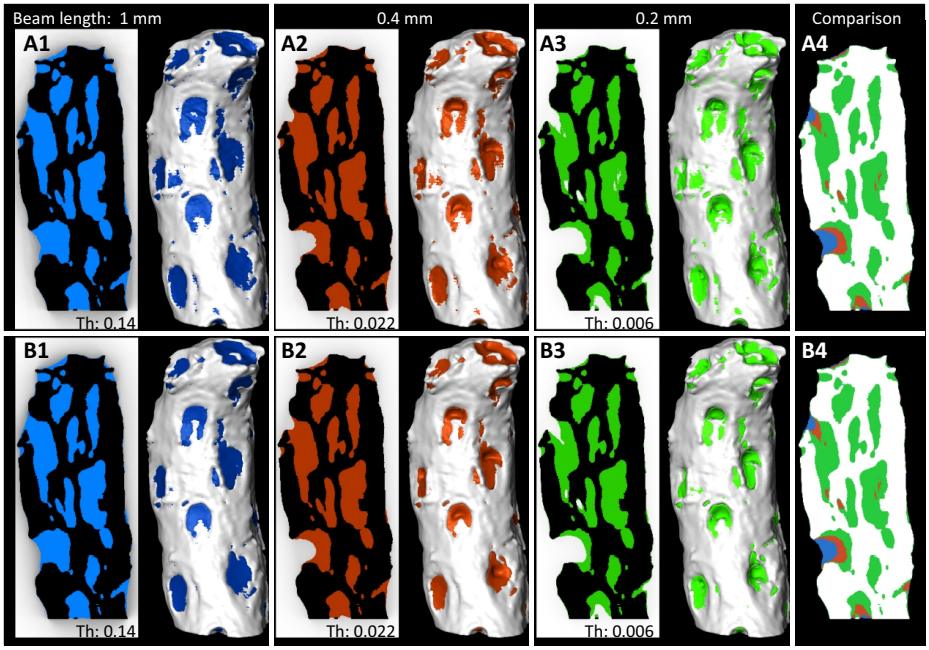

Figure 5. Comparison of the threshold (Th) segmentation based on the ambient occlusion eigenvalue 1 field calculated with the original ambient occlusion algorithm (A1 - A3; Baum and Titschack, 2016) and the improved ambient occlusion algorithm introduced herein (B1 - B3) including the influence of the ray length on the segmentation result. For colour-coding see Figure 3.

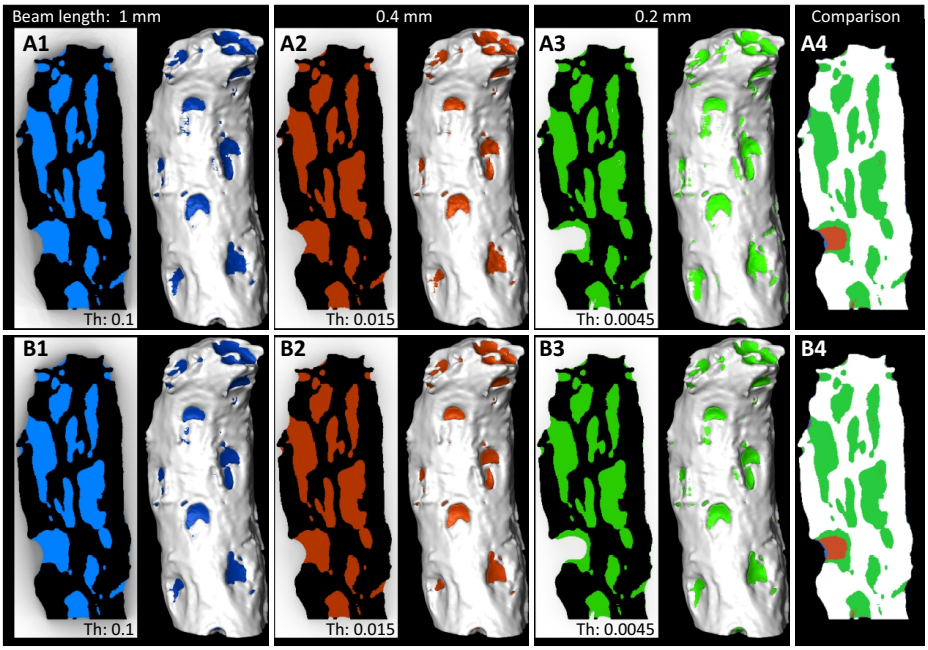

Figure 6. Comparison of the threshold (Th) segmentation based on the ambient occlusion eigenvalue 2 field calculated with the original ambient occlusion algorithm (A1 - A3; Baum and Titschack, 2016) and the improved ambient occlusion algorithm introduced herein (B1 - B3) including the influence of the ray length on the segmentation result. For colour coding see Figure 3.

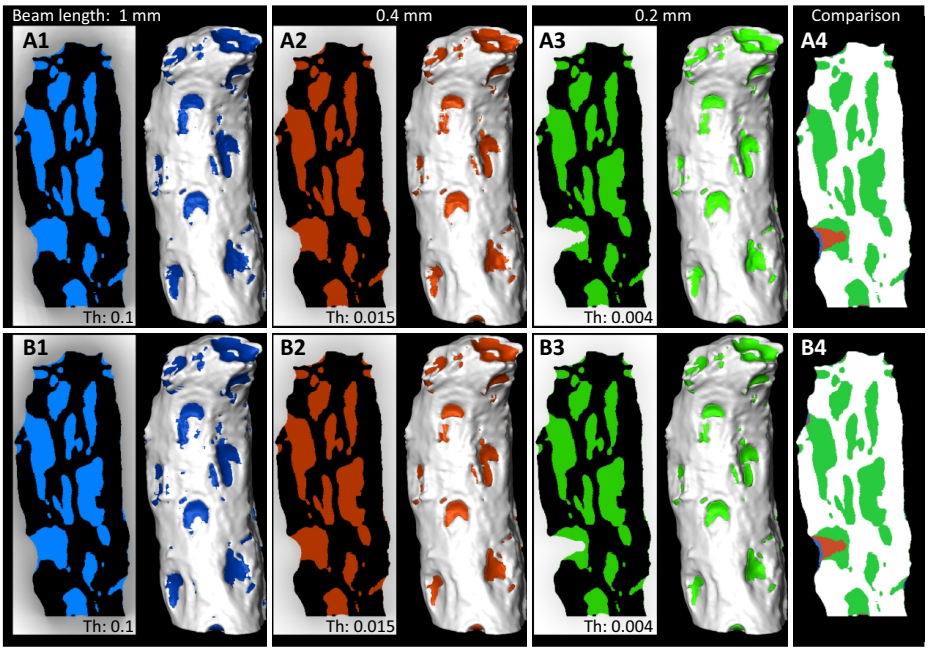

Figure 7. Comparison of the threshold (Th) segmentation based on the ambient occlusion eigenvalue 3 field calculated with the original ambient occlusion algorithm (A1 - A3; Baum and Titschack, 2016) and the improved ambient occlusion algorithm introduced herein (B1 - B3) including the influence of the ray length on the segmentation result. For colour coding see Figure 3.

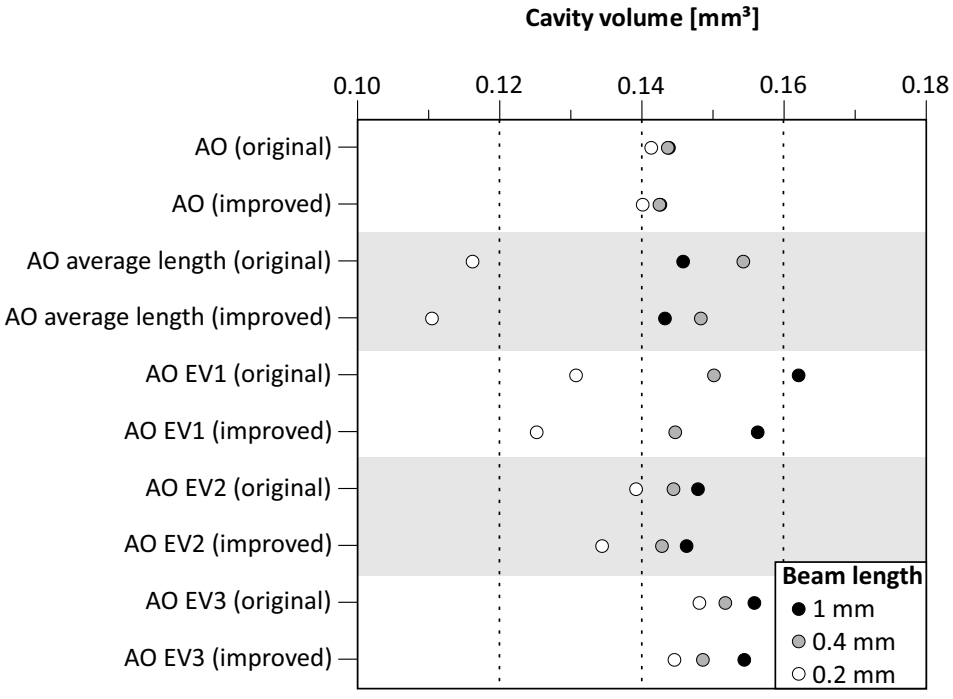

Figure 8. Comparison of determined cavity volumes based on the ambient occlusion field and ambient occlusion-derived fields calculated with the 'original' or 'improved' ambient occlusion algorithm and variable ray lengths between 0.2 and 1 mm. AO: ambient occlusion. EV = eigenvalue.

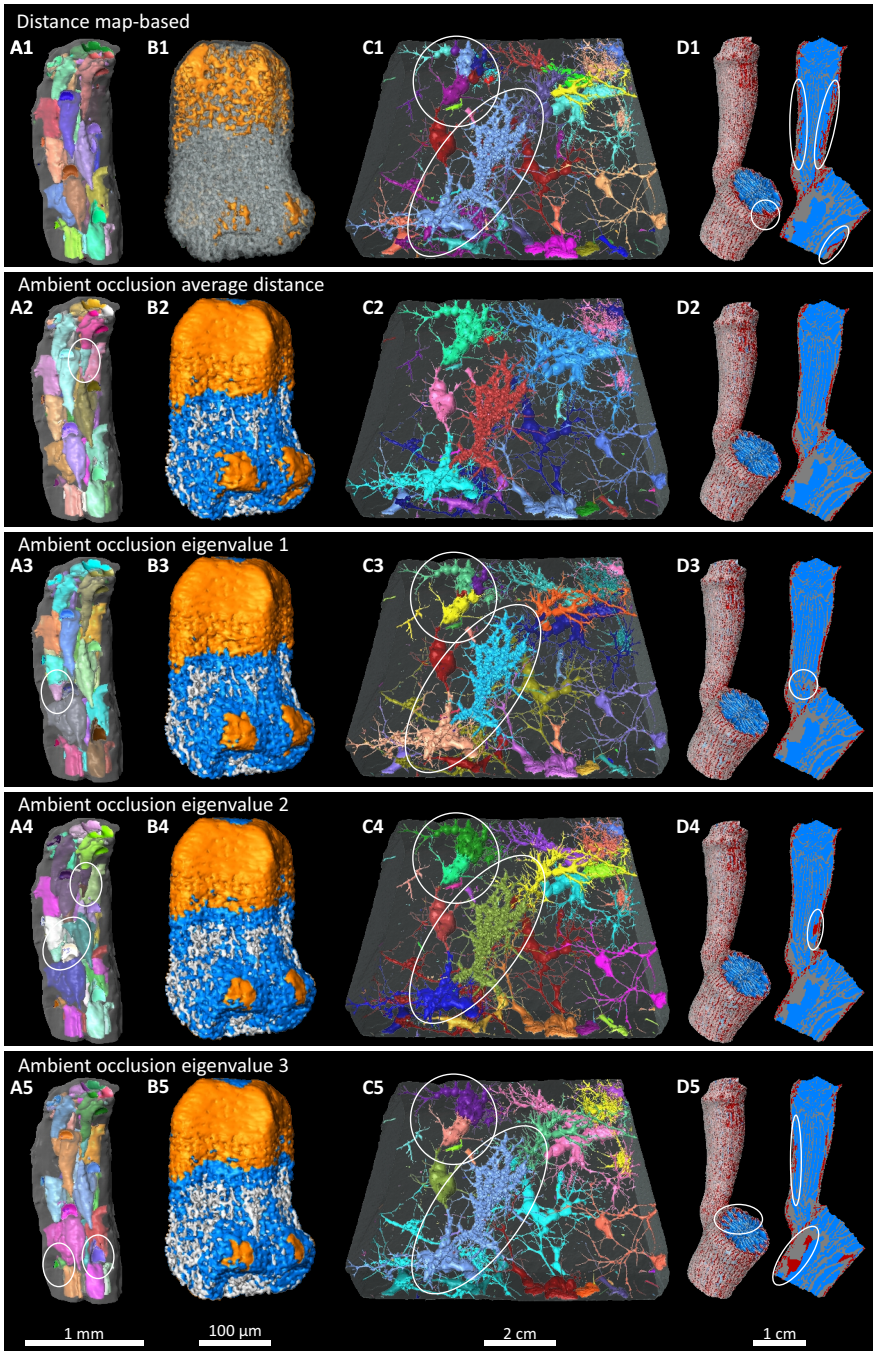

Figure 9. Segmentation results (A) of the zooid separation within the bryozoan *Cellaria bafouri* by the *ContourTreeSegmentation* module; (B) the stereom thickness classification of a tooth of the ophiuroid *Amphiura filiformis* (orange: compact; blue: moderate; grey: porous) by threshold segmentation; (C) the bioerosion trace separation within a bioeroded marble block by *ContourTreeSegmentation* module; (D) and the calice-pore separation within the dendrophyllid coral *Dendrophyllia* sp. using the marker-based *WatershedSegmentation* module (left: 3D model; right: orthoslice). Skeleton and marble block surfaces are shown in transparent grey (except B2 – B5). All segmentations were tested on distance map (A1 - D1), ambient occlusion average distance (A2 - D2), ambient occlusion eigenvalue 1 (A3 - D3), ambient occlusion eigenvalue 2 (A4 - D4), and ambient occlusion eigenvalue 3 fields (A5 - D5). Misclassifications/-separations are indicated by white circles.